On the Potential of Image Similarity Metrics for Comparing Phase Center Corrections

Johannes Kröger, Tobias Kersten, Yannick Breva, and Steffen Schön

Abstract

For highly precise and accurate positioning and navigation with Global Navigation Satellite Systems (GNSS), it is mandatory to take phase center corrections (PCC) into account. These corrections are provided by different calibration facilities and methods. Currently, discussions in the framework of the International GNSS Service (IGS) antenna working group (AWG) are ongoing on how to accept new calibration facilities as an official IGS calibration facility.

In this paper, different image similarity measures and their potential for comparing PCC are presented. Currently used comparison strategies are discussed and their performance is illustrated with several geodetic antennas. We show that correlation coefficients are an appropriate measure to compare different sets of PCC since they perform independently of a constant part within the patterns. However, feature detection algorithms like the Speeded-Up Robust Features (SURF) mostly do not find distinctive structures within the PCC differences due to the smooth character of PCC. Therefore, they are inapplicable for comparing PCC. Singular Value Decomposition (SVD) of PCC differences (ΔPCC) can be used to analyse which structures ΔPCC are composed of. We show that characteristic structures can be found within ΔPCC. Therefore, the SVD is a promising tool to analyse the impact of PCC differences in the coordinate domain.

Keywords

Image similarity metrics · Multi-GNSS processing · Phase center corrections · Singular value decomposition

1 Introduction

In order to obtain highly precise and accurate positioning and navigation solutions with Global Navigation Satellite Systems (GNSS), it is mandatory to take all error sources adequately into account. This includes phase center corrections (PCC) which are composed of a phase center offset (PCO) and azimuth- and zenith-dependent phase center variations (PCV). Due to the relative character of GNSS measurements, i.e. pseudoranges, a constant part r can additionally be present. The PCO is projected onto the unit line-of-sight vector $\boldsymbol{e}$ towards a satellite k with azimuth angle α and zenith angle z

$$PCC(\alpha^k, z^k) = -PCO \cdot \boldsymbol{e}(\alpha^k, z^k) + PCV(\alpha^k, z^k) + r. \tag{1}$$

PCC are provided by different facilities and calibration methods. Nowadays, the absolute correction values for receiver antennas are either determined in an anechoic chamber (Görres et al. 2006; Becker et al. 2010; Zeimetz 2010; Caizzone et al. 2021) or in the field by use of a robot (Bilich et al. 2018; Willi et al. 2019; Wübbena et al. 2019; Dawidowicz et al. 2021; Kröger et al. 2021; Wanninger et al.

J. Kröger (✉) · T. Kersten · Y. Breva · S. Schön
Leibniz Universität Hannover, Hannover, Germany

J. T. Freymueller, L. Sánchez (eds.), *Geodesy for a Sustainable Earth*,
International Association of Geodesy Symposia 154, https://doi.org/10.1007/1345_2022_146

2021) and are published in the Antenna Exchange (ANTEX) file (Rothacher and Schmid 2010).

Since newer GNSS frequencies (e.g. GPS L5) or systems, like Galileo or Beidou, are increasingly used in multi-GNSS processing and therefore added in the ANTEX file, there is the need for appropriate comparison strategies. Additionally, new calibration facilities want to contribute to the International GNSS Service (IGS) antenna working group (AWG). To this end, discussions are currently ongoing on what basis (parameters, thresholds, validation strategies, etc.) new calibration facilities should be accepted. This underlines the need of appropriate PCC comparison strategies.

The paper is structured as follows: Sect. 2 presents the different representation types of PCC and states the feasibility of image similarity metrics for comparing PCC. Section 3 shows the currently used comparison strategies based on different antenna types. In Sect. 4, global image similarity measures and their potential for comparing PCC are introduced. Section 5 deals with feature detection algorithms and their advantages and drawbacks for comparing PCC. Section 6 presents the singular value decomposition and its use in the context of PCC. Finally, Sect. 7 closes the paper with conclusion.

2 Representation of PCC

Usually, PCC are parametrized and estimated by use of spherical harmonic (SH) functions. Subsequently, the PCC are mapped on a regular grid with a typical step size of 5° azimuth α and 5° zenith angle z.

Figure 1 shows two different representation types of GPS L1 PCC for a geodetic choke ring antenna, widely used at reference stations (LEIAR25.R3 LEIT). The corrections values reach a magnitude of 160 mm. Since the Up-component of the PCO has the biggest impact (158.67 mm), a clearly elevation-dependent behaviour is detectable.

Figure 1a depicts the PCC in a stereographic projection, Fig. 1b on a regular grid. As it can be clearly seen in the latter figure, the PCC can be interpreted as a two-dimensional image. In this case, the actual grey-scale value of a pixel x_{ij} is equivalent to the metric correction value PCC(α, z). Therefore, image similarity metrics can principally be used to compare PCC.

3 Current Comparison Strategies

Currently, different sets of PCC (PCC_A, PCC_B) are mainly compared by computing the differences at the pattern level. In this paper, whenever differences of two PCC sets ΔPCC are analysed, the individually estimated PCC between the calibration method `Chamber` and `ROBOT` are studied

$$\begin{aligned} \Delta PCC &= PCC_A - PCC_B \\ &= PCC_{CHAMBER} - PCC_{ROBOT}. \end{aligned} \tag{2}$$

The following analyses are carried out with the individually estimated PCC for different antennas listed in Table 1. All of them are used in the EUREF Permanent GNSS Network (EPN) (Bruyninx and Legrand 2017). Note, that for `PCC6` – a TRM15990 SCIS antenna – no individual calibration is available for method `ROBOT` so that the type mean values are used instead.

Since PCO and PCV cannot be considered separately, it is important to take the full sets of PCC for comparisons into account as they contain all information. Moreover, a constant part r may be present which results from the PCC datum definition or the strategy applied to estimate PCO and PCV. If only small PCC differences $PCV_{A,B}$ should be analysed, the different sets can be transformed to a common PCO set (Menge et al. 1998)

$$\begin{aligned} PCV_{A,B}(\alpha, z) = (PCO_B - PCO_A) \cdot \boldsymbol{e}(\alpha, z) + \\ PCV_A(\alpha, z) + \Delta r. \end{aligned} \tag{3}$$

If the constant parts $r_{A,B}$ are not explicitly known, Δr can not be taken separately into account but may be present within $PCV_{A,B}$. With Eq. 3 different sets of PCV ($\widetilde{\Delta PCV}$) can be compared

$$\widetilde{\Delta PCV} = PCV_{A,B} - PCV_B. \tag{4}$$

Figure 2a shows only elevation-dependent GPS L1 differences by calculating the mean value per 5° azimuth bin. In addition, the minimum and maximum absolute difference per bin are depicted in dashed lines. The differences are shown for two cases: (i) blue-coloured original ΔPCC and (ii) red-coloured constrained ΔPCC, so that the PCC are zero at zenith (z = 0). This is equal to subtracting a constant value from one of the pattern, which is a valid transformation of PCC (Schön and Kersten 2013).

In Fig. 2a it can be clearly seen that the differences are larger for the non-constrained ΔPCC at low and middle zenith angles ($z \leq 80°$). Here, the differences are in the range of 0.8 mm to 1.7 mm whereas the differences for the constrained ΔPCC are between −0.9 mm and 0.2 mm.

In the past, a rule of thumb was applied by the IGS that deviations between sets of PCC of the same antenna have to be smaller than 1 mm beneath 80° zenith angles of only zenith-dependent pattern. However, for this example the goal is only achieved for the constrained ΔPCC.

Figure 2b shows the absolute ΔPCC in a cumulative histogram. Here, zenith- and azimuth dependent PCC are

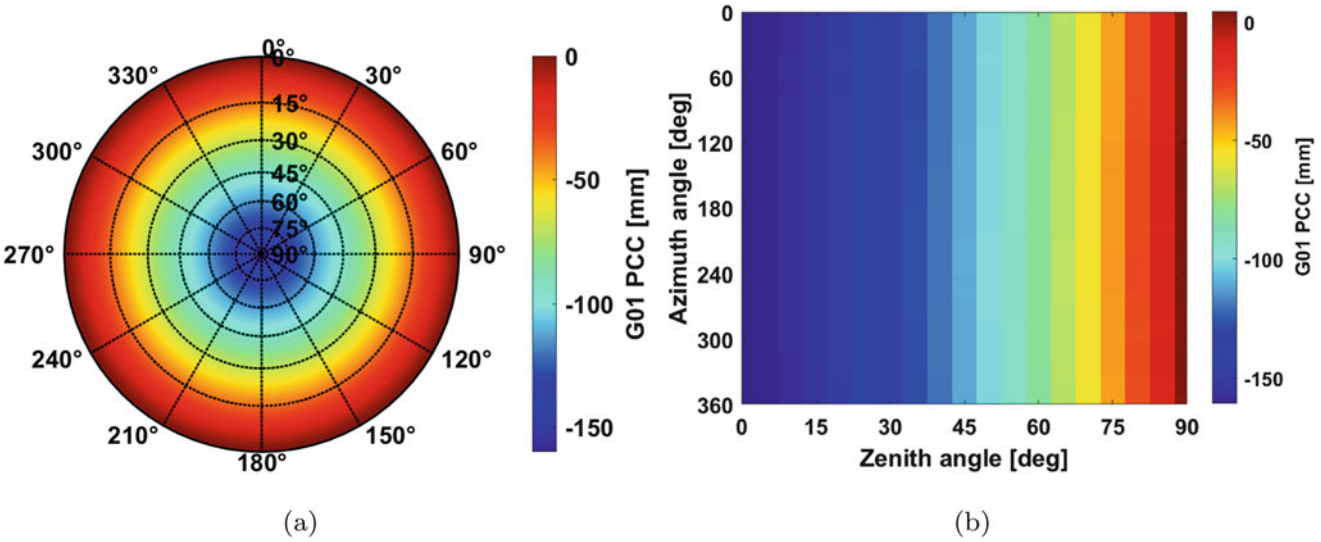

Fig. 1 Different representations of GPS L1 (G01) PCC of a LEIAR25.R3 LEIT antenna (denoted as `PCC1` in Table 1) as (**a**) stereographic projection and (**b**) grid view

Table 1 Individually calibrated antennas (methods `CHAMBER` & `ROBOT`) used for PCC comparison analyses

ID	Antenna name	Radom	Serial number
`PCC1`	LEIAR25.R3	LEIT	09390011
`PCC2`	LEIAR25.R3	LEIT	09050002
`PCC3`	LEIAR25.R4	LEIT	08500021
`PCC4`	LEIAR25.R4	LEIT	725072
`PCC5`	LEIAR25.R3	NONE	09300021
`PCC6`	TRM15990	SCIS	5744338072[a]

[a] Only type mean PCC for method `ROBOT`

considered. Again, the red-coloured constrained ΔPCC show lower deviations compared to the non-constrained blue-coloured ΔPCC. While 73 % of the constrained ΔPCC are below 1 mm, for the non-constrained ΔPCC these are only 33 %. Both representations underline the need of a more detailed guideline of the comparison.

Table 2 shows the characteristic values for the depicted ΔPCC of `PCC1`. The maximum, the Root Mean Square (RMS) and a certain threshold, e.g. stating percentage of $\Delta\text{PCC} < 1$ mm, depend on the constant value r within the PCC. The standard deviation, range [1] and spread [2], however, are independent of r.

Furthermore, the characteristic values shown here give higher numbers when the PCC are not zero-zenith constrained. This underlines the need of taking possible different PCC datum definitions or the strategy how to separate PCO and PCV during the analysis of the calibration adequately into account.

[1] range = max(ΔPCC) - min(ΔPCC)

[2] spread = range(PCC_A) - range(PCC_B)

Although the spread performs independently from a constant part, it should be noted that the measure changes if a transformation as shown in Eq. 3 is performed.

Moreover, a currently used comparison strategy is the investigation of the impact of ΔPCC in the coordinate domain as shown in Willi et al. (2019) and Kröger et al. (2021). In this case, the comparisons cannot be immediately interpreted since the achieved results are heavily dependent on the used processing strategy, e.g. cutoff angles, tropospheric models, observations weights, station location, used systems and signals, etc.

4 Global Image Similarity Measures

In this section, two global image similarity measures are exemplary analysed w.r.t their applicability to compare different sets of PCC. While the big advantage is that only one metric describes the similarity, the drawback is that the spatial structure of the ΔPCC gets lost. However, this is needed if the impact in the coordinate domain should be analysed in detail.

4.1 Correlation Coefficients

Correlation coefficients give the similarity between two sequences of numbers and vary typically between -1 and $+1$, whereas $c = +1$ is called *perfect positive correlation* (Goshtasby 2012).

Here, the feasibility of using the Pearson correlation coefficient c to compare different sets of PCC is exemplarily studied. Since each pattern PCC_s is normalised with respect

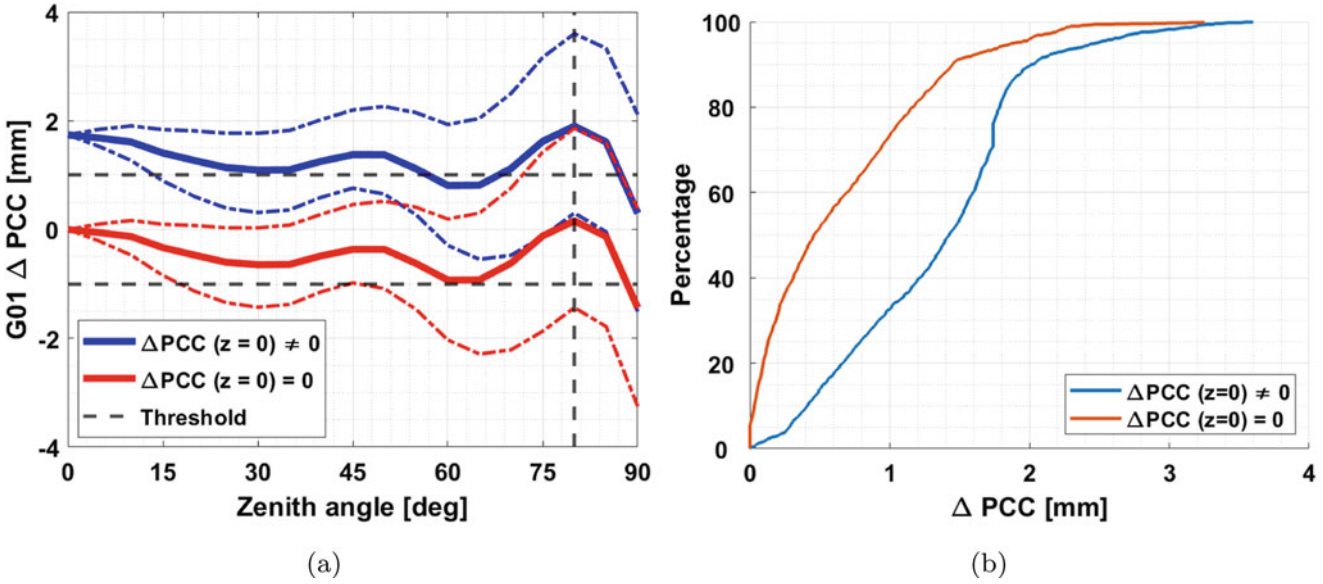

Fig. 2 Representation of ΔPCC (method CHAMBER - ROBOT) of a LEIAR25.R3 LEIT antenna (PCC1 in Table 1) as (**a**) zenith dependent ΔPCC and (**b**) in a cumulative histogram of absolute ΔPCC

Table 2 Characteristic values for ΔPCC of PCC1

Characteristic value	Non-constrained	Constrained
Maximum	3.60 mm	3.25 mm
RMS	1.49 mm	0.89 mm
Threshold (<1 mm)	32.59 %	73.40 %
Standard deviation	0.76 mm	
Spread	1.78 mm	
Range	3.63 mm	

to its standard deviation σ_s and mean value $\overline{PCC_s}$, c performs independently of r_s (Goshtasby 2012)

$$c = \frac{1}{n}\sum_{i=1}^{n}\left(\frac{(PCC_A - \overline{PCC}_A)}{\sigma_{PCC_A}}\right)\cdot\left(\frac{(PCC_B - \overline{PCC}_B)}{\sigma_{PCC_B}}\right). \quad (5)$$

Since the PCO_{Up} component is the most dominating part in PCC (cf. Fig. 1), PCC sets of the same antenna are quite similar so that the coefficients give usually high correlations.

Therefore, different sets of PCC need to be transformed to a common PCO beforehand, following Eq. 3. Subsequently, Table 3 shows the Pearson correlation coefficients for the original ΔPCC and the transformed ones ($\Delta\widetilde{PCV}$). For both differences, height offsets ΔH of 5 mm and 10 mm have been additionally added to one of the pattern so that the corresponding change of c can be seen. While c gives values close to one for ΔPCC, the $sin(\Delta H)$ offsets are clearly

Table 3 Similarity of non-transformed ΔPCC and transformed $\Delta\widetilde{PCV}$ expressed by Pearson correlation coefficient c for PCC1

Scenario	ΔH [mm]	ΔPCC	$\Delta\widetilde{PCV}$
Original ΔPCC	0	0.9998923	0.9450931
PCC_A + sin ΔH	5	0.9998917	0.8592048
PCC_A + sin ΔH	10	0.9998896	0.7682259

projected into the correlation coefficient for the transformed $\Delta\widetilde{PCV}$.

Figure 3a shows the relation between the absolute maximum value of $\Delta\widetilde{PCV}$ and c. Here, the numbers are given for $\Delta\widetilde{PCV}$ constrained to zero in zenith (depicted by squares) and non-constrained $\Delta\widetilde{PCV}$, illustrated by circles. Therefore, it can be again clearly seen that the maximum – as a characteristic value for describing the similarity between different sets of PCC – do not perform independently from a constant value r. Moreover, it gets clear that the $\Delta\widetilde{PCV}$ can be quite similar by means of c although the maximum value states a low similarity. As an example serves PCC6. Here, the highest deviation in terms of the maximum value is – as expected – present since an individual calibration is compared with the type mean calibration. On the other hand, the maximum deviation may indicate a high similarity of $\Delta\widetilde{PCV}$ while the correlation coefficient gives a low similarity, cf. PCC3.

The same conclusions can be drawn from Fig. 3b, where the relation between c and the RMS of $\Delta\widetilde{PCV}$ is illustrated. The highest similarity can again be observed for PCC5, the lowest similarity for PCC6.

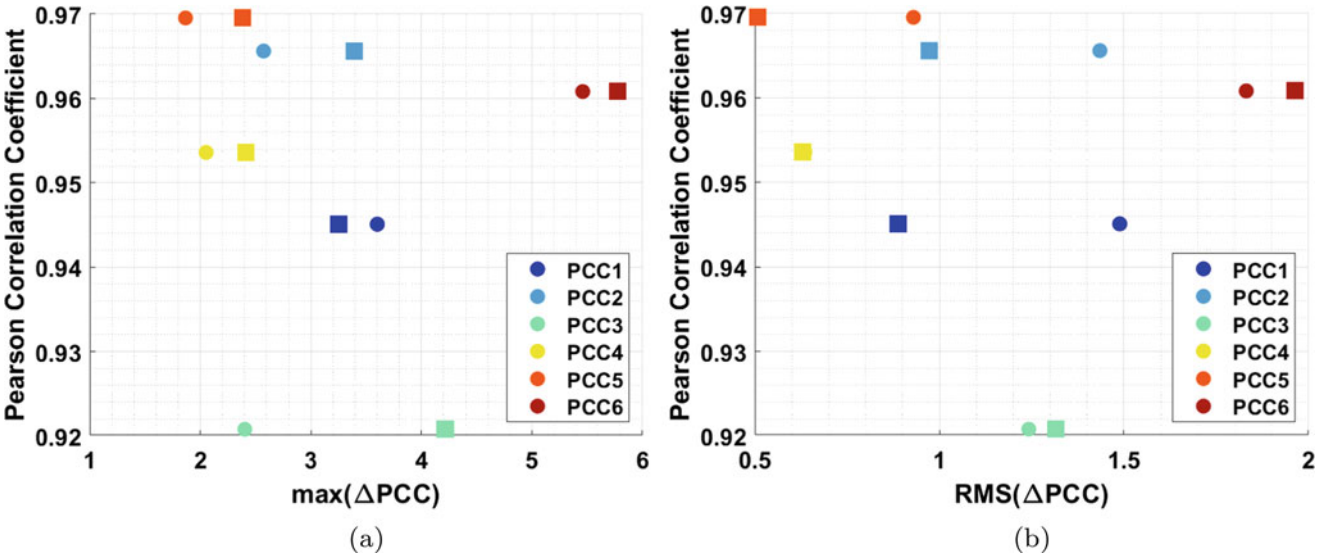

Fig. 3 Relations between Pearson correlation coefficient c and (**a**) maximum differences and (**b**) RMS of $\Delta\widetilde{PCV}$. Zero zenith constrained $\Delta\widetilde{PCV}$ are shown by squares, non-constrained $\Delta\widetilde{PCV}$ by circles

4.2 Structural Similarity Index

The Structural SIMilarity (SSIM) index introduced by Wang et al. (2004) measures the similarity of an input image w.r.t. a reference image. Since it is not only constrained to image processing but can also used as a similarity measure for comparing any two signals, it can be used to compare different sets of PCC. However, they need to be rescaled beforehand, since the input signals have to be non-negative.

The SSIM is composed of three components so that an overall similarity measure S(x,y) is achieved

$$S(x, y) = f(l(x, y), c(x, y), s(x, y)) \tag{6}$$

with x indicating in our case PCC_A and y denoting PCC_B, each pattern rescaled to the interval [0 1].

The function l(x,y) compares the luminance by mainly comparing the mean values of the input signals. The term c(x,y) is a contrast comparison by comparing the standard deviations of each pattern. The function s(x,y) is a structure comparison which normalises the signals w.r.t their standard deviations. All three terms contain constants (C1, C2, C3) to avoid instabilities. Moreover, each function can be weighted to adjust its relative importance.

In accordance with Wang et al. (2004), following constants have been used for the investigations carried out in this contribution: $C1 = 1 \cdot 10^{-4}$, $C2 = 9 \cdot 10^{-4}$, C3 = C2/2. The weights have been chosen to 1 so that consequently all terms have the same influence on S.

Figure 4a shows the relation between S and the maximum differences of $\Delta\widetilde{PCV}$. Again, zero zenith constrained $\Delta\widetilde{PCV}$ are shown by squares, non-constrained $\Delta\widetilde{PCV}$ by circles. It can be seen that the SSIM is not affected by a constant value within the PCC and that the index performs overall similar to c (cf. Fig. 3a). However, especially for `PCC6` S states a lower similarity compared to c. The same conclusions can be drawn from Fig. 4b, where the relation between S and the RMS of $\Delta\widetilde{PCV}$ is shown.

All in all, the SSIM is a very powerful measure to compare different sets of PCC. However, a change of the parameters (C_k and weights) and the corresponding impact on S needs further investigations. Thanks to its ease of application the Pearson correlation coefficient could be used for comparisons of PCC since it gives principally the same conclusions.

5 Feature Detection Algorithms

Feature detection algorithms are widely used to find distinctive and corresponding points in two images of the same scene. According to Bay et al. (2008), they can be divided into three main steps: (i) detection of *interest points* like corners or blobs, (ii) representation of the *interest point*'s neighbourhood by a feature vector – known as the *descriptor* – and (iii) matching of the *descriptors* between different images.

In the context of comparing PCC, feature detection algorithms could be used to find blobs in ΔPCC which would indicate larger PCC differences in a certain area. Figure 5

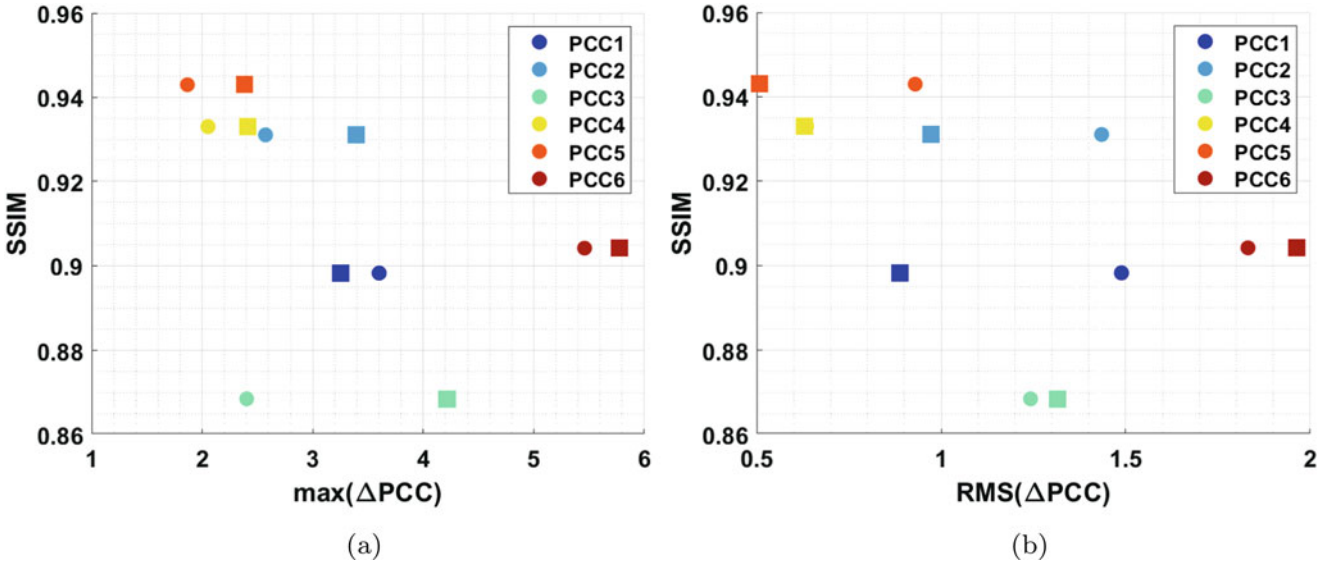

Fig. 4 Relations between SSIM S and (**a**) maximum differences and (**b**) RMS of $\Delta\widetilde{PCV}$. Zero zenith constrained $\Delta\widetilde{PCV}$ are shown by squares, non-constrained $\Delta\widetilde{PCV}$ by circles

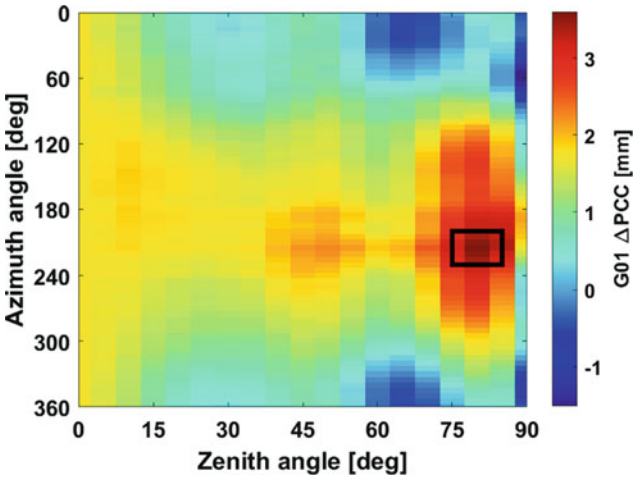

Fig. 5 ΔPCC1

shows the ΔPCC of PCC1. The black rectangle highlights a local structure which could be detected by a feature detection algorithm.

We used the Speeded-Up Robust Features (SURF) algorithm in order to find blobs in ΔPCC. It is a scale- and rotation-invariant detector and descriptor proposed by Bay et al. (2008). Our analyses have shown that the so-called blob features are mainly not detected since PCC are due to estimation by SH quite smooth. Moreover, the PCC resolution of 5° steps makes a detection quite hard because fine structures get lost. Also taking the $\Delta\widetilde{PCV}$ as the input image or carrying out a rescaling of the differences to the interval [0 1] does not lead to a successful result by use of the SURF algorithm.

6 Singular Value Decomposition

The Singular Value Decomposition (SVD) is a widely used tool for e.g. matrix characterisation, data reduction or the solving of nearly singular linear equations (Stewart 1993; Wall et al. 2003). Here, in the context of comparing PCC, SVD can be used to express the ΔPCC as the product of the three matrices **U**, **S** and **V**, whereas the matrix **S** contains the singular values s_i on the main diagonal

$$\Delta PCC = U \cdot S \cdot V^T = \sum_{i=1}^{n} u_i \cdot s_i \cdot v_i^T = \sum_{i=1}^{n} M_i \qquad (7)$$

The SVD can be used to analyse which structures ΔPCC are composed of and to investigate if structures are present within ΔPCC, which could be neglected. It is an approximation of the ΔPCC data matrix in terms of the Frobenius norm. The rectangular data matrix represents a map of the hemisphere. It should be noted that each grid point contributes equally to the Frobenius norm, although grid points at high zenith angles represents a larger area of the spherical segment. This is a general drawback of the commonly used mapping method for PCC.

Figure 6 shows the differences between the complete ΔPCC1 and the summation of SVD results of ΔPCC1 up to M_4 in a cumulative histogram. If the first four SVD structures are summed up, most of the ΔPCC information is kept since the differences to the full ΔPCC are smaller than 0.2 mm. All other structures can be assumed to be neglectable.

This is also underlined by Fig. 7, which depicts these findings for different antennas. In Fig. 7a, the magnitude of the singular values s_i are shown. For all samples, the first singular value s_1 contains by far the most information.

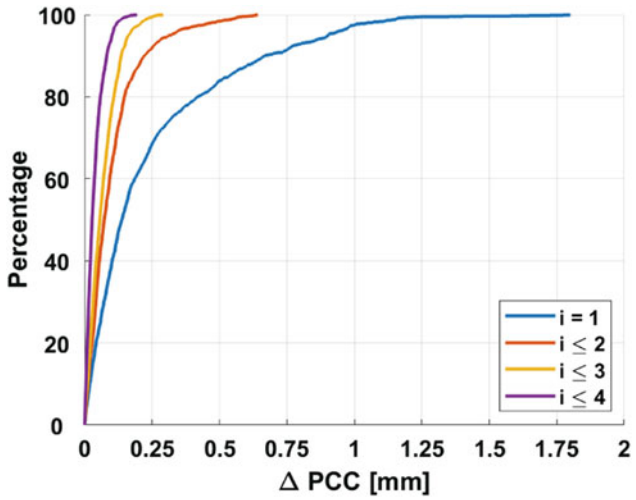

Fig. 6 SVD of ΔPCC1

Figure 7b illustrates the differences between the full ΔPCC set and the first four structures ($s < 5$, cf. Eq. 7) in a cumulative histogram. These structures contain almost all ΔPCC information since the differences to the full ΔPCC are below 0.25 mm.

Figure 8 shows simulated ΔPCC with different introduced offsets for the PCO. In Figs. 8a–c one offset has been introduced: 5 mm for the horizontal components North (N) and East (E), 160 mm for the horizontal Up component (U). In Figs. 8e and f offsets for all three PCO components have been introduced, using the above-mentioned order of magnitudes. While for the first cases all pattern information is contained in M_1, for the latter case M_1 and M_2 contain these structures.

Clearly visible structures can be found for all cases. They depend on the respective trigonometrical functions for calculating the PCO. Therefore, for example, the negative North offset of 5 mm is present for azimuth angles 0° and 360° and zenith angle 90°, see Fig. 8a. Keep in mind the changed sign of the PCO within the PCC, cf. Eq. 1.

Figures 9, 10, 11, 12 show the SVD of ΔPCC up to M_4 for four of the six different antennas introduced in Table 1 (PCC1, PCC2, PCC5, PCC6). For all examples, it can be clearly seen that the order of magnitude decreases with increasing degree of the singular value s. Please note the different scales for the colour-coded ΔPCC. This representation is chosen so that small structures for the different antennas are detectable.

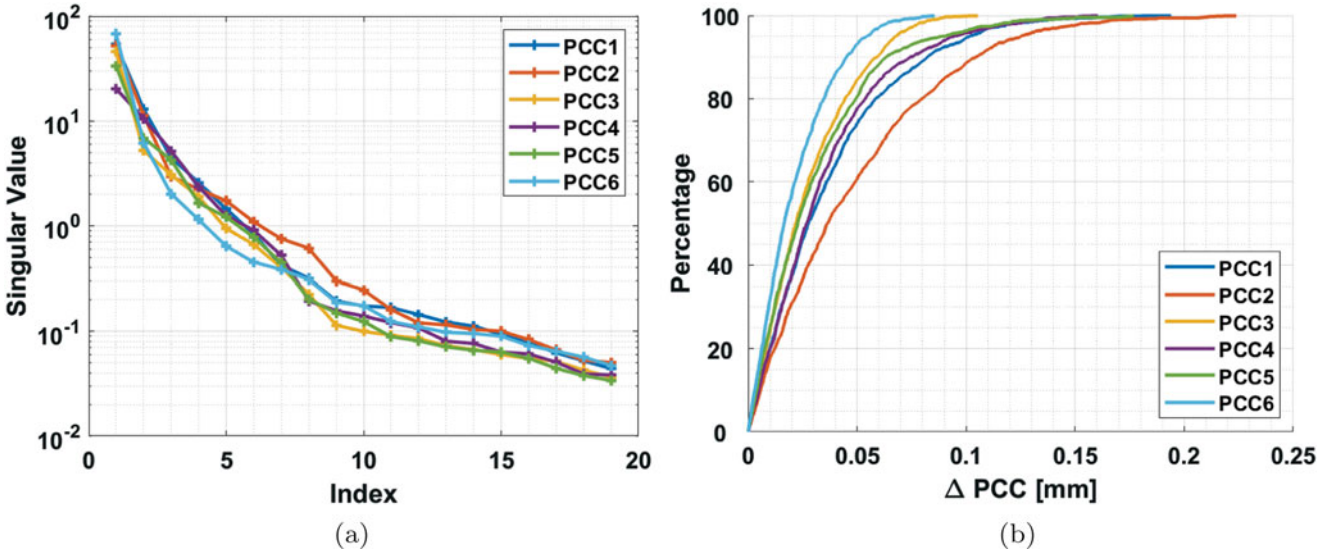

Fig. 7 SVD results for different antenna types showing (**a**) the magnitude of singular values s_i and (**b**) differences between full ΔPCC and summation of individual structures up to M_4, cf. Table 1

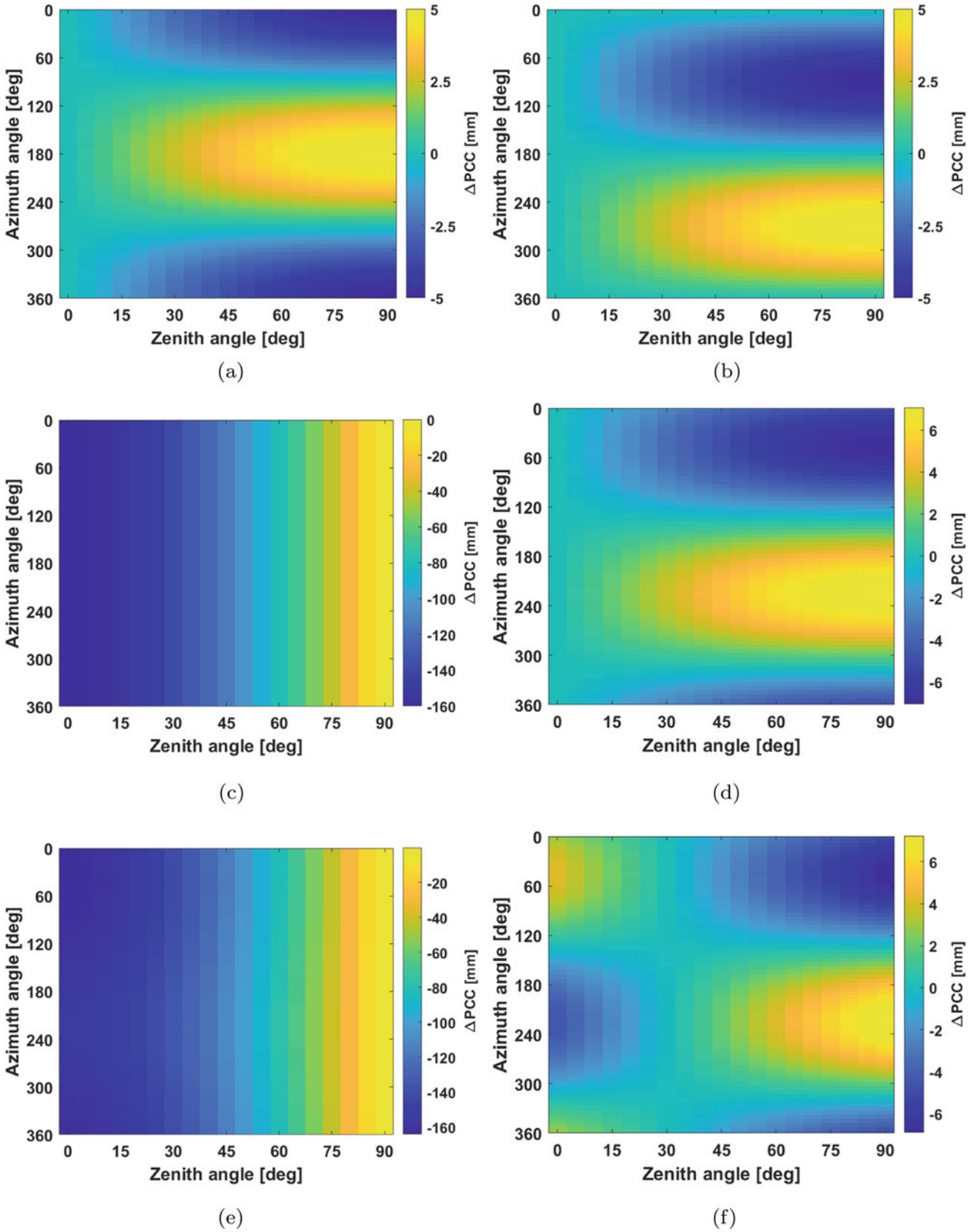

Fig. 8 SVD of simulated PCC with introducing different PCO offsets. (**a**) M_1, N = 5 mm, M_1, E = 5 mm. (**b**) M_1, U = 160 mm. (**c**) M_1, N = E = 5 mm. (**d**) M_1, N = E = 5 mm, U = 160 mm. (**e**) M_2, N = E = 5 mm, U = 160 mm

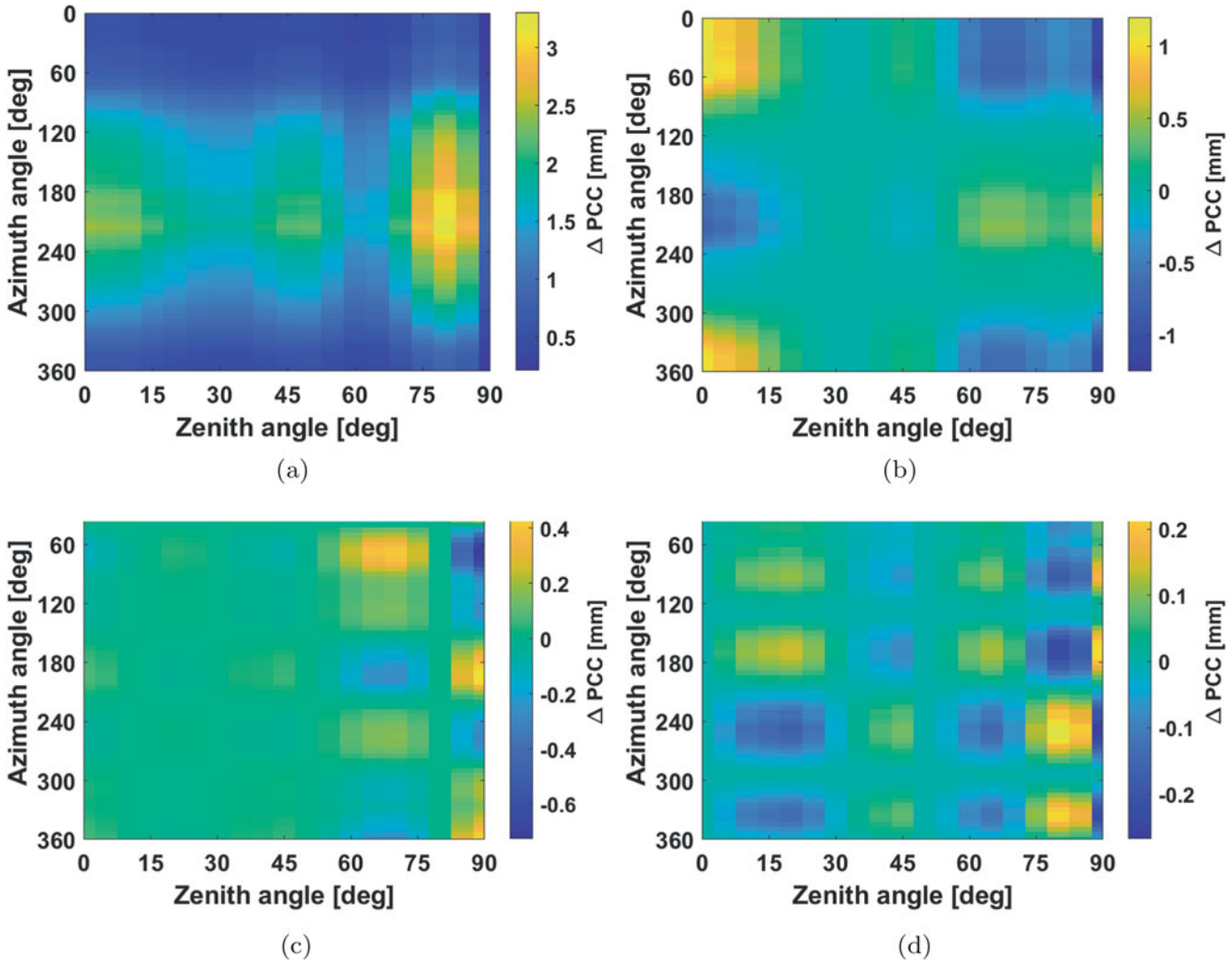

Fig. 9 SVD of ΔPCC1 (LEIAR25.R3 LEIT). (**a**) M_1. (**b**) M_2. (**c**) M_3. (**d**) M_4

A higher similarity between the different antennas is observable with increasing degree i. For example, a chessboard behaviour is detectable for M_4 for all antennas. This incisive structure can also be found partly in M_3, e.g. visible in Fig. 9c at high zenith angles, in Fig. 10c or in Fig. 11c. This chessboard structure is to some extent related to the chosen degree and order of the SH expansion. Since the used parameters are usually not reported, a detailed analysis of the relation between number of zero crossings and degree and order of the SH expansion cannot be carried out here, but needs further investigation. It is worth noticing that this structure was also used by Geiger (1988) as a specific antenna type in order to analyse analytically the impact in the position domain. This underlines that the SVD can be a promising tool for error propagation from pattern level to position domain.

If the SVD results of PCC1 in Fig. 9 are compared to the full difference pattern shown in Fig. 5, the main structures are reflected in M_1. Actually, the advantage of SVD gets clear when having a look on M_2, since this structure would otherwise not be detectable. By comparing M_2 (Fig. 9b) with M_2 of the simulated PCC in Fig. 8f, an overall comparable structure is observable. This could indicate, that the ΔPCC of PCC1 includes a larger offset in at least one of the horizontal PCO components, i.e. North or East. Although a single comparison of the PCO components without taking the corresponding PCV into account for comparing different sets of PCC is not fully correct, it can give a first idea of the differences. In this case, ΔN = 1.18 mm which could explain the structure and order of magnitude of M_2. However, some parts of this structures could additionally be present in M_1, M_3 or M_4.

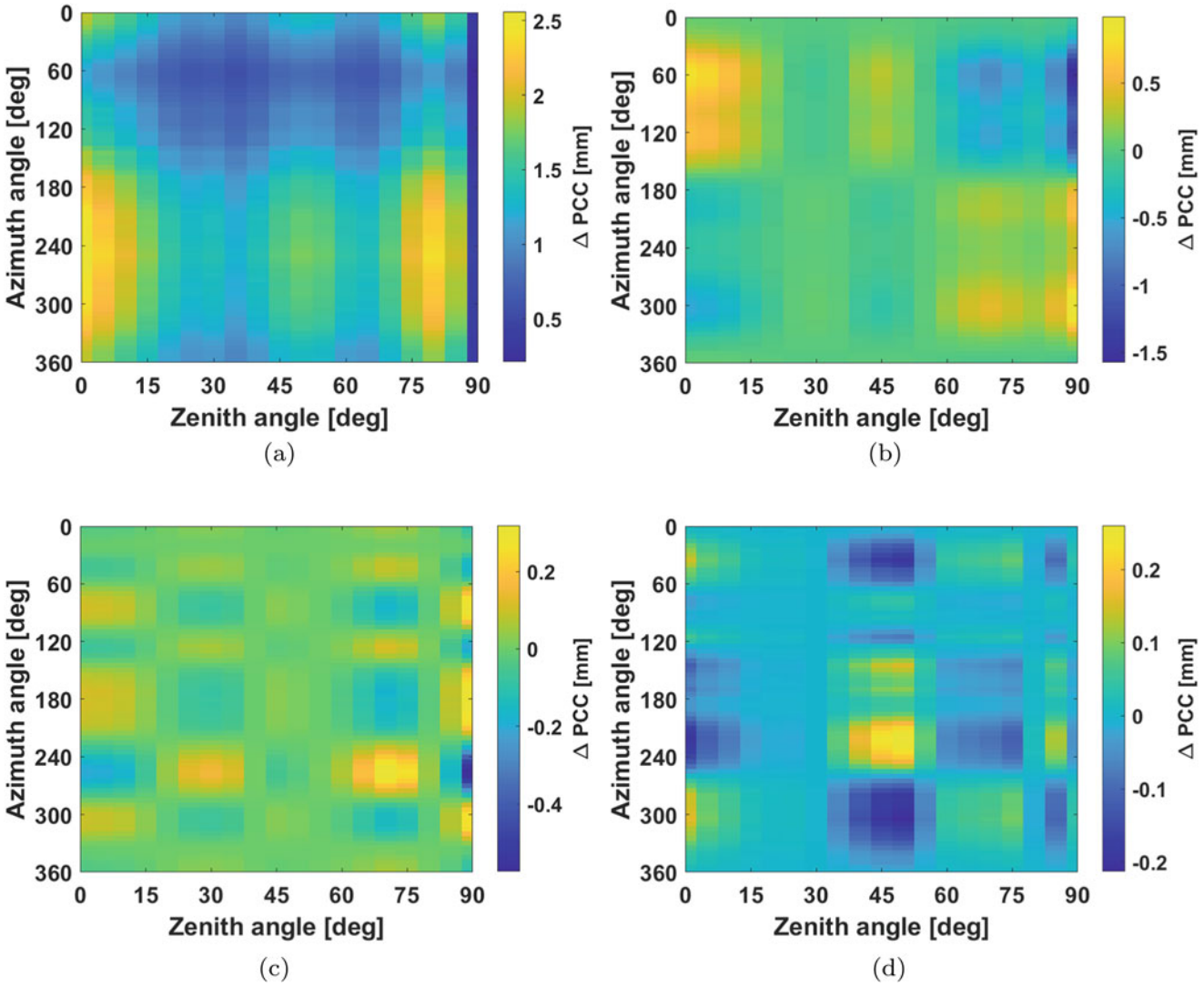

Fig. 10 SVD of ΔPCC2 (LEIAR25.R3 LEIT). (**a**) M_1. (**b**) M_2. (**c**) M_3. (**d**) M_4

Another behaviour of the simulated PCC can be detected in Fig. 12a for M_1. In this case, a clear PCO-Up offset can be seen, similar to the one shown in Figs. 8c and e. This is reflected as mainly zenith-dependent differences in M_1.

7 Conclusion

In this paper, we presented the potential of image similarity metrics for comparing PCC. We showed that the Pearson correlation coefficient c is an appropriate way to measure the similarity of different PCC sets by a scalar quantity. However, it needs to be transformed beforehand to a common PCO. We demonstrated that c is independent of a constant part within the pattern and that it is – compared to the powerful SSIM – easy to use. Additionally, the results were compared w.r.t. widely used comparison metrics like the RMS or maximum deviation of ΔPCC.

Our analyses of SURF, as an example for a feature detection algorithm, showed that mostly distinctive structures within ΔPCC are not found. This is due to the smooth character of the PCC.

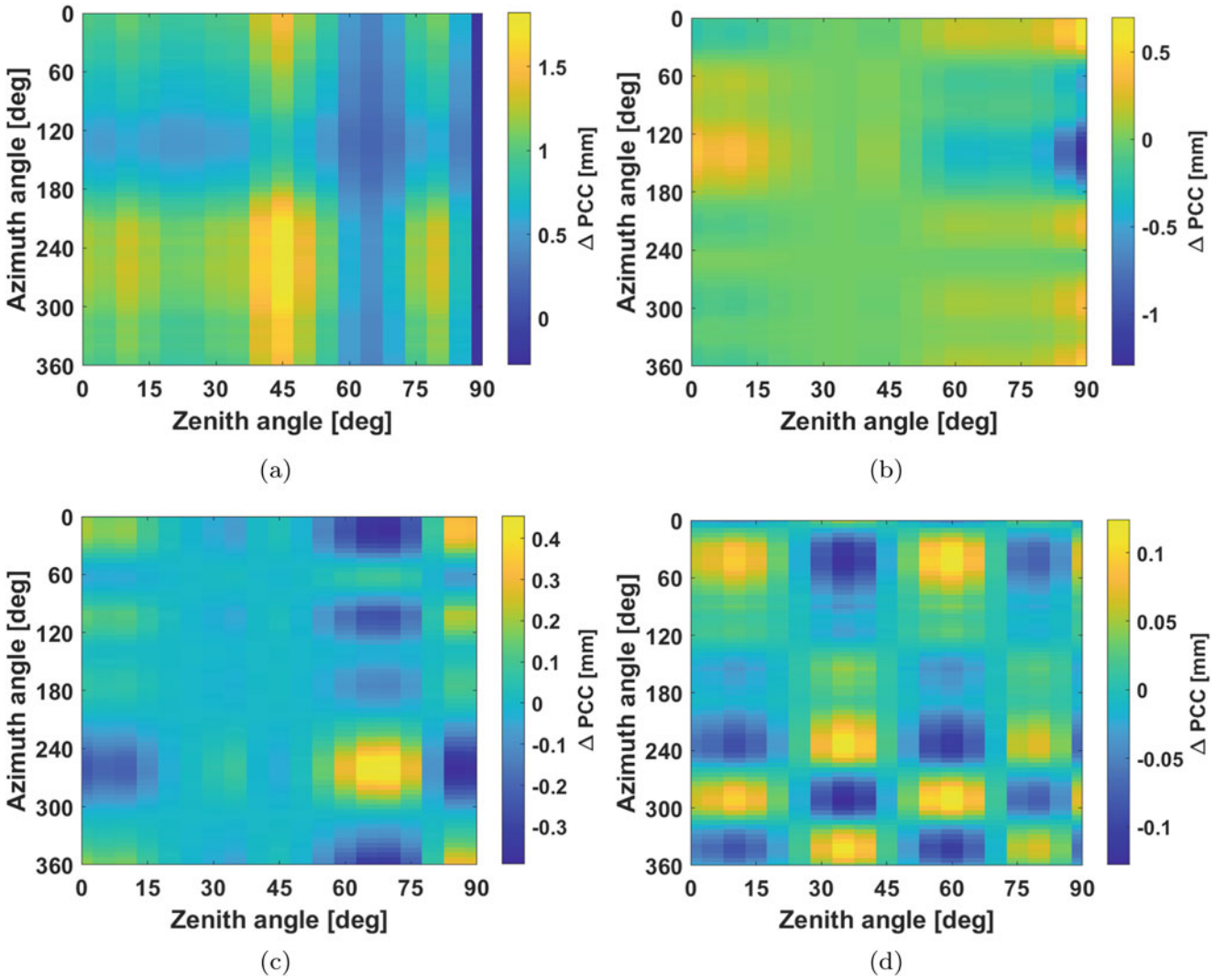

Fig. 11 SVD of ΔPCC5 (LEIAR25.R3 NONE). (**a**) M_1. (**b**) M_2. (**c**) M_3. (**d**) M_4

On the other hand, SVD of ΔPCC can be a promising tool to analyse the impact of PCC differences from the pattern level to the coordinate domain. We illustrated that recurring structures can be found in the differences, i.e. offsets in the horizontal or vertical PCO components. Moreover, a chessboard structure is mostly found within the pattern, which is most probably linked to the used degree and order of the SH synthesis.

In future, a detailed analysis of the relation between the chessboard structures and the SH synthesis need to be carried out. Furthermore, the obtained structures should be used to assess the impact in the coordinate domain. Our findings are a good basis for this, since almost all pattern information (Δ <0.25 mm) is contained within the first four degrees of the SVD. Therefore, the complex structures of PCC can be simplified.

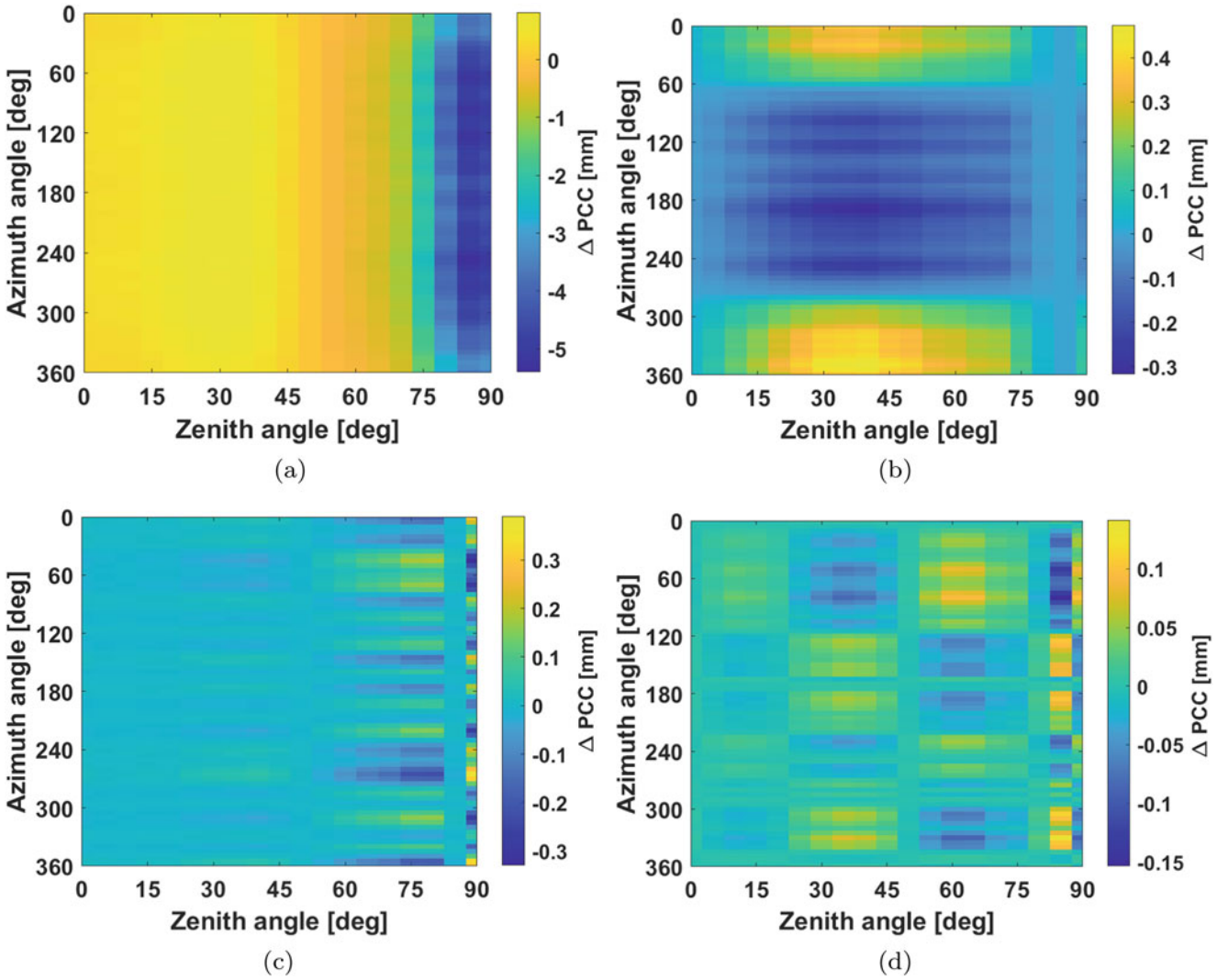

Fig. 12 SVD of ΔPCC6 (TRM15990 SCIS). (**a**) M_1. (**b**) M_2. (**c**) M_3. (**d**) M_4

Acknowledgements The authors would like to thank Franz Rottensteiner from the Institute of Photogrammetry and Geoinformation (IPI) for valuable comments and fruitful discussions on different image similarity metrics.

References

Bay H, Ess A, Tuytelaars T, Van Gool L (2008) Speeded-Up Robust Features (SURF). Comput Vis Image Underst 110(3):346–359. https://doi.org/10.1016/j.cviu.2007.09.014

Becker M, Zeimetz P, Schönemann E (2010) Anechoic Chamber calibrations of phase center variations for new and existing GNSS signals and potential impacts in IGS processing. In: Presentation at the IGS Workshop 2010 and vertical rates symposium, June 28–July 2, Newcastle, United Kingdom of Great Britain

Bilich A, Mader G, Geoghegan C (2018) 6-axis robot for absolute antenna calibration at the US National Geodetic Survey. In: Presentation at the IGS workshop 2018, October 29–November 2, Wuhan, China, poster

Bruyninx C, Legrand J (2017) Receiver antenna calibrations available from the EPN CB. In: EUREF AC workshop, October 25-26, Brussels, Belgium

Caizzone S, Schönfeldt M, Elmarissi W, Circiu MS (2021) Antennas as precise sensors for GNSS reference stations and high-performance PNT applications on earth and in space. Sensors 21(12). https://doi.org/10.3390/s21124192

Dawidowicz K, Rapiski J, Smieja M, Wielgosz P, Kwasniak D, Jarmolowski W, Grzegory T, Tomaszewski D, Janicka J, Gołaszewski P, Wolak B, Baryla R, Krzan G, Stepniak K, Florin-Catalin G, Brzostowski K (2021) Preliminary results of an Astri/UWM EGNSS receiver antenna calibration facility. Sensors 21(14). https://doi.org/10.3390/s21144639

Geiger A (1988) Modeling of phase center variation and its influence on GPS-positioning. In: Groten E, Strauss R (eds) GPS-techniques applied to geodesy and surveying, proceedings of the international GPS-workshop Darmstadt, April 10 to 13, 1988, vol 19. Springer, pp 210–222. https://doi.org/10.1007/bfb0011339

Goshtasby AA (2012) Image registration: Principles, tools and methods. Springer Science & Business Media. https://doi.org/10.1007/978-1-4471-2458-0

Görres B, Campbell J, Becker M, Siemes M (2006) Absolute calibration of GPS antennas: Laboratory results and comparison with field and robot techniques. GPS Solutions 10(2):136–145. https://doi.org/10.1007/s10291-005-0015-3

Kröger J, Kersten T, Breva Y, Schön S (2021) Multi-frequency multi-GNSS receiver antenna calibration at IfE: Concept - calibration results - validation. Adv Space Res. https://doi.org/10.1016/j.asr.2021.01.029

Menge F, Seeber G, Völksen C, Wübbena G, Schmitz M (1998) Results of the absolute field calibration of GPS antenna PCV. In: Proceedings of the 11th international technical meeting of the Satellite Division of The Institute of Navigation (ION GPS 1998), September 15–18, Nashville, TN, USA, Institute of Navigation, IEEE, pp 31–38

Rothacher M, Schmid R (2010) ANTEX: The antenna exchange format, Version 1.4. Tech. rep.

Schön S, Kersten T (2013) On adequate comparison of Antenna Phase Center variations. In: Presentation at the American Geophysical Union, Annual Fall Meeting 2013, December 09.–13., San Francisco, CA, USA

Stewart GW (1993) On the early history of the singular value decomposition. SIAM Review 35(4):551–566

Wall ME, Rechtsteiner A, Rocha LM (2003) Singular value decomposition and principal component analysis. In: A practical approach to microarray data analysis. Springer, pp 91–109

Wang Z, Bovik A, Sheikh H, Simoncelli E (2004) Image quality assessment: from error visibility to structural similarity. IEEE Trans Image Process 13(4):600–612. https://doi.org/10.1109/TIP.2003.819861

Wanninger L, Thiemig M, Frevert V (2021) Multi-frequency quadrifilar helix antennas for cm-accurate GNSS positioning. J Appl Geodesy. https://doi.org/10.1515/jag-2021-0042

Willi D, Lutz S, Brockmann E, Rothacher M (2019) Absolute field calibration for multi-GNSS receiver antennas at ETH Zurich. GPS Solutions 24(1). https://doi.org/10.1007/s10291-019-0941-0

Wübbena G, Schmitz M, Warneke A (2019) Geo++ absolute multi frequency GNSS antenna calibration. In: Presentation at the EUREF Analysis Center (AC) Workshop, October 16–17, Warsaw, Poland

Zeimetz P (2010) Zur Entwicklung und Bewertung der absoluten GNSS-Antennenkalibrierung im HF-Labor. PhD thesis, Institut für Geodäsie und Geoinformation, Universität Bonn